

crease. The liquid cloud and rain particles cannot produce the enhanced delay, because the precipitating clouds would have to be more than 21 km deep to account for the maximum observed delay of 64 mm. The observed features in the interferogram illustrate how localized areas with an increased water vapor content may give an indication for the occurrence and development of precipitation.

The interferogram in Fig. 4 illustrates the frequently occurring phenomenon of horizontal convective rolls, a form of boundary-layer convection in which there are counter-rotating horizontal vortices with axes aligned along the mean boundary-layer wind direction (27, 28). Some evidence that the linear features of the interferogram depict rolls rather than atmospheric waves is that the bands are oriented along the wind direction, as shown by the surface station data overlaid on the interferogram (Fig. 4A). Moreover, radiometer satellite imagery (Fig. 4B) to the south of the interferogram location shows some evidence of cloud streets oriented with the interferogram bands. Sufficient moisture in the presence of rolls often produces cloud streets atop roll updraft branches (29). Furthermore, a local radiosonde on 4 April 1996 at 12:00 UTC indicated a boundary-layer depth of 800 m. This result, combined with the band spacing of 2 to 3 km, gives an aspect ratio of 2.5 to 2.9, consistent with the presence of rolls (30).

Roll updrafts are warmer and moister than roll downdraft branches (5). Moisture variability is likely dominant in the observed 6- to 10-mm delay differences, because vapor pressure variations associated with rolls (3 hPa) would produce a delay of 13 mm, whereas temperature variations of 0.5°C would produce less than a 1-mm delay. The observations show how streets of water vapor can be identified even when cloud streets are not visible. In fact, no clouds were observed from the weather stations in the interferogram area. Knowledge of these systematic patterns of water vapor can aid in forecasting weather behavior.

Radar interferometry can provide worldwide coverage of mesoscale atmospheric phenomena over land and ice, and easily monitor more exotic features such as gravity waves accompanying fronts. Readily attainable integrated precipitable water amounts over large areas may make pinpoint weather forecasting a possibility. The delay maps could eventually be used by bench forecasters or serve as an additional constraint in variational data assimilation models. Contemporary satellites, however, have an orbital repeat period that is far from ideal for operational applications (31), resulting in the loss of coherent phase information over many areas. Proper use of airborne and spaceborne SAR systems with short repeat periods could lead to much greater accuracy in meteorological understanding and forecasting.

References and Notes

1. D. Rind et al., *Nature* **349**, 7500 (1991).
2. K. Emanuel et al., *Bull. Am. Meteorol. Soc.* **76**, 1194 (1995).
3. N. A. Crook, *Mon. Weather Rev.* **124**, 1767 (1996).
4. C. K. Mueller, J. W. Wilson, N. A. Crook, *Weather Forecasting* **8**, 132 (1993).
5. T. M. Weckwerth, J. W. Wilson, R. M. Wakimoto, N. A. Crook, *Mon. Weather Rev.* **124**, 769 (1996).
6. H. A. Zebker, C. L. Werner, P. A. Rosen, S. Hensley, *IEEE Trans. Geosci. Remote Sensing* **32**, 823 (1994).
7. Interferometric phase differences are derived by differencing radar backscatter measurements at the wavelength level, so that if the surface changes on the order of centimeters between observations, the measurement is corrupted (32). Because water surfaces are completely different at the centimeter scale for time differences of hours or days, as set by orbital repeat cycles, no meaningful data can be acquired over the ocean.
8. H. A. Zebker and R. M. Goldstein, *J. Geophys. Res.* **91**, 4993 (1986).
9. A. K. Gabriel and R. M. Goldstein, *Int. J. Remote Sensing* **9**, 857 (1988).
10. A. K. Gabriel, R. M. Goldstein, H. A. Zebker, *J. Geophys. Res.* **94**, 9183 (1989).
11. D. Massonnet et al., *Nature* **364**, 138 (1993).
12. D. Massonnet, P. Briole, A. Arnaud, *ibid.* **375**, 567 (1995).
13. R. Goldstein, *Geophys. Res. Lett.* **22**, 2517 (1995).
14. D. Massonnet and K. L. Feigl, *ibid.*, p. 1537.
15. H. Tarayre and D. Massonnet, *ibid.* **23**, 989 (1996).
16. H. A. Zebker, P. A. Rosen, S. Hensley, *J. Geophys. Res.* **102**, 7547 (1997).
17. J. Saastamoinen, *Bull. Geodesique* **106**, 383 (1972).
18. J. L. Davis, T. A. Herring, I. I. Shapiro, A. E. E. Rogers, G. Elgered, *Radio Sci.* **20**, 1593 (1985).
19. G. Elgered, *IEEE Trans. Antennas Propag.* **AP-30**, 502 (1982).
20. Because the SAR phase can only be measured modulo 2π and the satellite position is not known to wave-
- length accuracy, only lateral gradients in signal delay can be observed. In addition, long wavelength delay gradients, caused by either orbit inaccuracies or hydrostatic or ionospheric gradients, are removed in the process of adjusting the interferogram to a local reference ellipsoid.
21. R. Hanssen, "Atmospheric heterogeneities in ERS tandem SAR interferometry," *Delft Institute for Earth-Oriented Space Research (DEOS) Rep. No. 98.1* (Delft Univ. Press, Delft, 1998).
22. D. Just and R. Bamler, *Appl. Opt.* **33**, 4361 (1994).
23. M. Bevis et al., *J. Geophys. Res.* **97**, 15787 (1992).
24. D. B. Parsons, *J. Atmos. Sci.* **49**, 1810 (1992).
25. J. E. Simpson, *Sea Breeze and Local Wind* (Cambridge Univ. Press, Cambridge, 1994).
26. E. R. Kursinski, G. A. Hajj, J. T. Schofield, R. P. Linfield, *J. Geophys. Res.* **102**, 23429 (1997).
27. M. A. LeMone, *J. Atmos. Sci.* **30**, 1077 (1973).
28. R. A. Brown, *Rev. Geophys. Space Phys.* **18**, 683 (1980).
29. M. A. LeMone and W. T. Pennell, *Mon. Weather Rev.* **104**, 524 (1976).
30. J. P. Kuettner, *Tellus* **23**, 404 (1971).
31. Ideally, SAR data should be acquired with multiple short temporal spacings in order to maintain high coherence and permit a large number of interferogram pairs to be generated. Multiple observations give not only better precision in time, but keep coherence and hence data quality high.
32. H. A. Zebker and J. Villasenor, *IEEE Trans. Geosci. Remote Sensing* **30**, 950 (1992).
33. We thank J. Wilson, J. Keeler, F. Fabry, V. Wulfmeyer, and two anonymous reviewers for their helpful comments and suggestions. The ERS SAR data were kindly provided by the European Space Agency and the meteorological data by the Royal Netherlands Meteorological Institute. The German Aerospace Research Establishment is acknowledged for assisting in the data processing.

4 November 1998; accepted 22 January 1999

Tropospheric Aerosol Climate Forcing in Clear-Sky Satellite Observations over the Oceans

J. M. Haywood,¹ V. Ramaswamy,^{2*} B. J. Soden²

Tropospheric aerosols affect the radiative forcing of Earth's climate, but their variable concentrations complicate an understanding of their global influence. Model-based estimates of aerosol distributions helped reveal spatial patterns indicative of the presence of tropospheric aerosols in the satellite-observed clear-sky solar radiation budget over the world's oceans. The results show that, although geographical signatures due to both natural and anthropogenic aerosols are manifest in the satellite observations, the naturally occurring sea-salt is the leading aerosol contributor to the global-mean clear-sky radiation balance over oceans.

Tropospheric aerosols (1, 2), which include sulfate (3, 4), black carbon (5, 6), organic carbon (6), mineral dust (7), and sea-salt (8, 9), affect Earth's radiation budget in a significant manner. Predictions of their net radiative effect have proven difficult because aerosol distributions

vary greatly in type, space, and time. By reflecting sunlight, the present-day background tropospheric aerosols reduce the solar radiation absorbed by the planet (10). Likewise, an increase in anthropogenic aerosols leads to additional reflection, and this has in turn led to a negative radiative forcing of climate change over the past century (1). A central issue underlying potential aerosol-climate linkages is verification of the presence of aerosols and their associated radiative effects, both in the context of the present-day climate and climate change scenarios.

¹Meteorological Research Flight, United Kingdom Meteorological Office, Farnborough, Hants GU14 0LX, UK. ²Geophysical Fluid Dynamics Laboratory, Princeton University, Princeton, NJ 08542, USA.

*To whom correspondence should be addressed. E-mail: vr@gfdl.gov

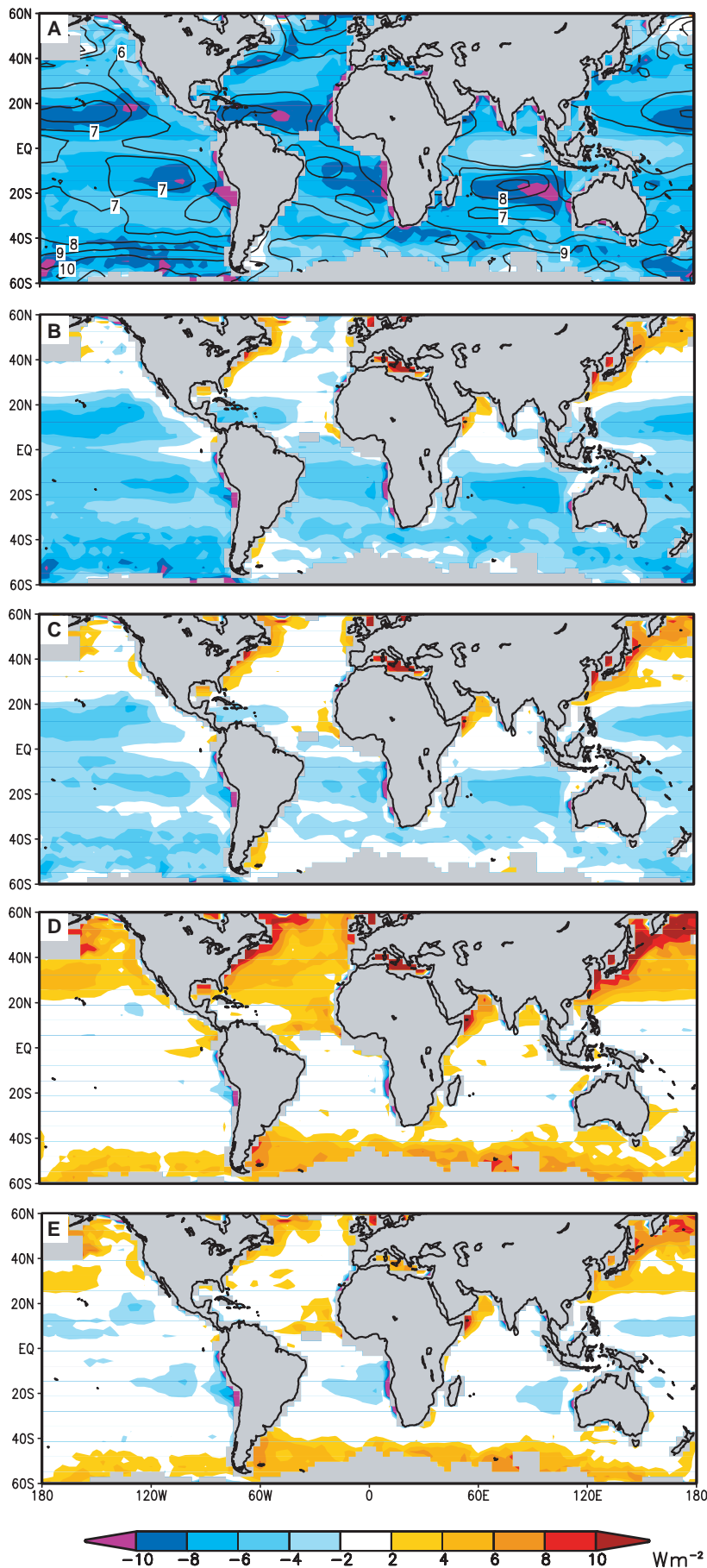


Fig. 1. Difference between GCM computations and ERBE satellite observations of the annual-mean solar irradiance reflected at the top of the atmosphere in clear skies over oceans, for different aerosol assumptions (see also Table 2). **(A)** With no aerosols considered in the model calculations; contours of surface wind speeds (in meters per second) as derived from SSMI data also indicated. **(B)** All aerosol types listed in Table 1, except sea-salt aerosols, are considered. **(C)** Same as (B) plus a low sea-salt burden estimate. **(D)** Same as (B) plus a high sea-salt burden estimate. **(E)** Same as (D), except the sulfate components are ignored in the calculations. Gray coloring indicates land regions and areas of missing data.

Here, we discerned the global radiative presence of tropospheric aerosols by focusing on the spatial pattern of the annual-mean, clear-sky, cloud-free reflected solar irradiance (11). We invoked the fundamental knowledge that aerosols scatter and absorb solar radiation. To identify the influence of aerosols, we compared the clear-sky, top-of-the-atmosphere (TOA) solar irradiances computed using a general circulation model (GCM) (12) with those observed by the Earth Radiation Budget Experiment (ERBE) satellite (11). In the first stage of the calculations, no aerosols were included. In the second stage, distributions of various aerosol species, as estimated from models, were used, and appropriate optical parameters were included to describe the radiative properties of each species. We considered only oceanic regions because the ocean albedo is relatively well characterized, whereas substantial uncertainties exist for land surface albedos.

Monthly-mean ERBE irradiances (11) and monthly-mean Special Sensor Microwave Imager (SSMI) surface wind speed data (13) over oceanic regions were computed over concurrent time periods (July 1987 until December 1988) to form composite monthly means. The GCM includes a well-calibrated solar radiative transfer scheme (14) and an improved parameterization of the ocean surface albedo based on observations (15). The model was integrated for 1 year and the monthly-mean TOA irradiances averaged to form an annual mean (16). Monthly-mean differences in the TOA irradiances between the GCM and ERBE observations were calculated and annual means obtained by appropriate averaging. Our analysis excluded areas with sea-ice in the GCM and where the monthly ERBE sampling frequency of clear skies was less than once every 2 days.

Monthly-mean fields for anthropogenic (4) and natural (3) sulfate, black carbon (5), and eight different size categories of mineral dust (8) were obtained from global aerosol climatologies estimated from three-dimensional chemistry-transport models (3D CTMs). Organic carbon climatologies are not yet generally available, so we used the distribution of black carbon (6) as a proxy along with a simple scaling between the masses of organic and black carbon from anthropogenic activity (17).

REPORTS

Table 1. Optical properties (specific extinction k_e , single-scattering albedo ω , and asymmetry factor g) of different aerosols at a wavelength of 0.55 μm , and their respective effects on the global-and-annual-mean, clear-sky net short-wave irradiances at the top-of-the-atmosphere (TOA) and surface in oceanic regions. While sea-salt is naturally derived, sulfate and dust have natural and anthropogenic components, with the rest being of anthropogenic origin.

Species	k_e (m^2/g)	ω	g	Irradiance	
				TOA (W/m^2)	Surface (W/m^2)
Natural sulfate	9.74	1.00	0.75	-0.93	-0.86
Anthropogenic sulfate	9.74	1.00	0.75	-0.72	-0.68
Organic carbon	8.04	1.00	0.75	-1.02	-0.96
Black carbon	9.26	0.21	0.34	+0.17	-1.12
Natural dust	*	*	*	-0.58	-1.10
Anthropogenic dust	*	*	*	-0.54	-1.07
Low sea-salt	2.5	1.00	0.78	-1.51	-1.55
High sea-salt	2.5	1.00	0.78	-5.03	-5.17

*The optical parameters in the case of natural and anthropogenic dust are based on a segregation of the aerosol distributions in terms of eight different classes. The parameters are approximately those used in (15).

The global annual-mean atmospheric burden of organic carbon was assumed to be 73.2 Tg (6).

The ubiquitous aerosol over the global oceans is sea-salt; its concentration varies with wind speed (mostly) and location (8, 9, 18). In our calculations, the concentration of these aerosols was related to the local surface wind speed (9). The effect of other physical factors is not well understood (18). Because observations suggest a considerable range in the effect of wind speed on sea-salt aerosol concentration, we used two different empirical formulas that encompass several reported observations (9, 18), designated as “low” and “high” sea-salt concentration cases, respectively (19). These cases likely represent the lower and upper bounds of the actual sea-salt concentration, which remains uncertain to at least a factor of 3. Monthly-mean wind speed data from SSMI observations were used to generate appropriate sea-salt aerosol concentrations at ambient relative humidities, and the aerosols were assigned a constant mass concentration throughout the well-mixed marine boundary layer, assumed to be the lowest kilometer of the atmosphere. The resulting global, annual-mean sea-salt column burden was $\sim 36.8 \text{ mg}/\text{m}^2$ for the high case and $7.5 \text{ mg}/\text{m}^2$ for the low case; these may be compared with a detailed model estimate of $22.4 \text{ mg}/\text{m}^2$ (8).

We determined the radiative properties of each of the aerosol species at a relative humidity of 80% (except for mineral dust and black carbon, which are assumed to be hydrophobic), typical of the oceanic boundary layer, using Mie scattering theory [see, for example, (12)] and by assuming that each of the aerosol species may be modeled by appropriate log-normal distributions and refractive indices (2, 20, 21). Thus, we converted the gamma distributions used in previous calculations for mineral dust aerosol (22) to log-normal distributions. Our estimates of the aerosol single-scattering properties (Table 1) are consistent with other studies (12, 17, 22–25). For sea-salt, we chose a single

value of the specific extinction that accounts approximately for the effects due to the entire size distribution consisting of the sub- and supermicrometer categories (18, 26). We ignored the effects of internal mixing on aerosol radiative effects.

Radiative transfer computations indicate that, among non-sea-salt aerosols, organics have the largest effect at the TOA followed by sulfates and dust (Table 1). Black carbon decreases the outgoing solar irradiance in contrast to the effect of the other aerosol species. Together, the non-sea-salt aerosols increase the modeled TOA reflected irradiance by $3.6 \text{ W}/\text{m}^2$. The modeled TOA irradiance increases substantially even when the lower estimate of the sea-salt burden is considered, whereas the corresponding value for the high sea-salt case exceeds that due to the rest of the species combined. The total anthropogenic contribution, assuming linear additivity, is $2.1 \text{ W}/\text{m}^2$. The total natural aerosol contribution is 3.0 or $6.5 \text{ W}/\text{m}^2$, depending on the sea-salt climatology; this range encompasses the estimate of $4.9 \text{ W}/\text{m}^2$ obtained for a different assumed climatology of maritime aerosols at 70% relative humidity (10). The model calculations also show that all aerosol species reduce the solar irradiance at the surface (Table 1). The sea-salt (-1.6 to $-5.2 \text{ W}/\text{m}^2$) and the non-sea-salt natural ($-2.0 \text{ W}/\text{m}^2$) and anthropogenic ($-3.8 \text{ W}/\text{m}^2$) aerosols are all estimated to contribute significantly. This irradiance reduction can lead to a suppression of evaporation and affect the temperature structure of the oceanic upper layers. In the case of dust and black carbon, the change at the surface is larger than that at the TOA because these aerosols absorb as well as scatter radiation. The total global-mean aerosol effect results in a surface solar irradiance reduction of 7.4 or $10.8 \text{ W}/\text{m}^2$, depending on the sea-salt burden.

The annual-mean, clear-sky reflected solar irradiance, as computed by the GCM with consideration of only the effects of the atmo-

Table 2. Differences between the GCM-computed and ERBE-observed hemispheric-mean and global-mean, clear-sky solar reflection at the top of the atmosphere when different assumptions are made about the presence of aerosols in the global, annual-mean marine atmosphere.

Case	NH (W/m^2)	SH (W/m^2)	Global (W/m^2)
A. No aerosols	-6.88	-6.62	-6.74
B. All aerosols, except sea-salt	-1.36	-4.52	-3.12
C. All aerosols, with low sea-salt	-0.05	-2.85	-1.61
D. All aerosols, with high sea-salt	+2.99	+1.04	+1.91
E. Aerosols, high sea-salt, sulfates masked	+0.64	-0.06	+0.25
F. Aerosols, low sea-salt, sulfates masked	-2.40	-3.95	-3.27

spheric gases and surface albedo, underestimates the ERBE observations (Fig. 1A). The differences exhibit coherent spatial patterns. Negative differences are evident practically throughout the world’s oceans and exceed $4 \text{ W}/\text{m}^2$ over vast areas, indicating that the GCM requires an additional reflecting component globally, over and above the reflection due to molecular scattering and surface albedo. This suggests an important role for tropospheric aerosols in explaining this discrepancy. The model-observation biases exceed the uncertainty for temporally averaged ERBE clear-sky solar irradiance measurements (estimated to be $<2 \text{ W}/\text{m}^2$) (27). Areas where the disagreement between ERBE and GCM is larger than $8 \text{ W}/\text{m}^2$ include oceans off the western coasts of South America, South Africa, Australia, and North Africa and the central Northern Pacific and off the coast of the southeastern United States. The global-mean bias ($-6.7 \text{ W}/\text{m}^2$) is similar to that determined by other studies (28) and is about equal in both hemispheres (Table 2). Biases of this order are of substantial significance in the context of climate and climate change (1). These discrepancies cannot be due to deficiencies or errors in accounting for any gaseous constituents such as water vapor (29).

Inspection of the corresponding patterns in surface wind speed (contours in Fig. 1A) reveals that areas with pronounced deficits in GCM-predicted reflectance coincide with areas of high surface winds ($>7 \text{ m/s}$), notably the southern Indian, Pacific, and Atlantic oceans and the central Pacific at 10° to 20°N (30). Likewise, the bias tends to be smallest in regions of low wind speeds (for example, the western Pacific and equatorial Indian oceans). This suggests that the missing reflection component is associated with the surface wind speed. The correlation between the bias in the reflected irradiance and wind speed is also ev-

ident in the zonal and interannual variability of these fields (31). However, in certain regions, particularly at higher latitudes and near-coastal regions, the bias exhibits little dependence on wind speed, suggesting there are contributions from other factors.

Inclusion of non-sea-salt aerosols (Table 1) in the GCM calculations (Fig. 1B) reduces the global-mean difference between the modeled and observed irradiances by about a factor of 2 (Table 2), indicating that non-sea-salt aerosols are an important contributor to the observed clear-sky solar reflection. Locally, the difference approaches zero over large areas of the Northern Hemisphere (NH) and is less than 6 W/m^2 over much of the tropics and Southern Hemisphere (SH). The smaller reduction in bias for the SH relative to that in the NH (Table 2) suggests that non-sea-salt aerosols are insufficient to account for all of the irradiance differences there. In some regions of the NH, the observed irradiance is overestimated, for example, the Gulf of Arabia, off the coast of eastern Asia, the eastern United States, and western North Africa.

Consideration of the low sea-salt aerosol burden along with other aerosols leads to a further improvement in the GCM calculations (Fig. 1C). In this case, the SH pattern exhibits a bias of less than 6 W/m^2 everywhere; more areas in the equatorial and SH oceans acquire a null bias compared with Fig. 1B, and the SH mean bias is reduced substantially (Table 2). Areas of overestimates in the NH (Fig. 1B) exhibit a slightly more positive bias when the low sea-salt aerosol concentration is considered, but the NH mean bias is almost zero. The global-mean bias (Table 2) indicates a considerable improvement over the case where only non-sea-salt aerosols were considered. Thus, even a low sea-salt burden is a significant contributor to reflection over the world's oceanic regions.

Inclusion of the high sea-salt burden can explain virtually all of the difference in the reflection in the SH, especially at the center of the ocean basins and poleward of 10°S (Fig. 1D), but leads to an overestimate in the mid-to-high latitude NH oceans (Table 2). The SH mean bias is also positive for this case but smaller in magnitude. The global-mean solar reflection is increased by about 3.5 W/m^2 compared with the low sea-salt case and increased by more than 5 W/m^2 compared with the non-sea-salt case (Table 2), underscoring the potentially large effect of sea-salt relative to the other aerosol types on present-day clear-sky solar reflection over oceans.

Observations suggest that, over oceans and in the presence of sea-salt particles, the sulfates may be effectively incorporated in the sea-salt aerosol (32). Thus, sulfates over oceans may not have a separate optical identity, and calculations that consider sea-salt and sulfate as separate components may be overestimating the

radiative forcing by double-counting the two aerosol types, particularly in regions of high surface wind speeds and high sulfate particle concentrations. We thus performed a sensitivity study by recomputing the irradiances for the conditions described for the case above (case D, Table 2), but we ignored the natural and anthropogenic sulfate components (which together contribute 1.65 W/m^2 to TOA reflection; Table 1). Because the sea-salt refractive indices are approximately similar to those for sulfate, and because observations indicate that sea-salt mass dominates the scattering (18, 32), the refractive index of the sea-salt-sulfate mixture is assumed to be the same as that for sea-salt. The net result is a reduction of the total aerosol optical depth, and hence, of reflection and radiative forcing. The resulting spatial pattern of the bias (Fig. 1E) indicates a good agreement between model and observations almost everywhere from 40°N to 40°S (within $\pm 4 \text{ W/m}^2$). The regions where the irradiance is overestimated in Fig. 1D, especially mid-latitude NH oceans, are noticeably smaller. The global-mean bias in this case is 0.3 W/m^2 , whereas the hemispheric biases are substantially less than 1 W/m^2 (Table 2).

This sensitivity calculation and comparison with observed irradiances suggest that the anthropogenic sulfate aerosol effect over the oceans may have been overestimated by global radiative forcing studies (1). However, the sulfate masking simulated here may only be one factor in the complex microphysics of maritime aerosols, and further detailed considerations of the physico-chemical properties of such mixtures are required. For example, if instead of the high sea-salt model, the low sea-salt model is used in the calculation of the masking of the sulfate component, the negative biases in Fig. 1C would increase and the global-mean bias would be -3.3 W/m^2 (case F, Table 2). Nonetheless, this bias is still an improvement over the no-aerosols case (-6.7 W/m^2).

In summary, by comparing radiative computations using model-derived estimates of natural and anthropogenic aerosol distributions with clear-sky satellite-measured solar irradiances over oceans, one can infer geographical patterns attributable to tropospheric aerosols. Conversely, accurate satellite measurements of solar reflection are potentially useful for estimating the radiative effects of aerosols. The bias in the annual, global-mean, clear-sky reflected solar irradiances between model calculations and observations is reduced by at least one-half in magnitude (from -6.7 to between -3.3 and $+0.25 \text{ W/m}^2$; Table 2) when tropospheric aerosol distributions are considered. The radiative effect of aerosols estimated here may be compared with the net global-mean estimate for clouds (-17 W/m^2) (18).

The satellite irradiances off the coasts of western Africa, the northeastern United

States and Asia, and in the Indian Ocean are suggestive of aerosol emissions from the land areas, which necessarily include a substantial anthropogenic aerosol component. In these regions, wind speeds are relatively low, and sea-salt concentrations and associated radiative effects are less. We find that estimates of anthropogenic aerosol components (Table 1) are needed to explain the observed irradiances (Table 2). This lends credibility to the notion that such aerosols are key factors in the forcing of climate change (1), and that the clear-sky global short-wave satellite record likely includes the radiative signatures of these different anthropogenic aerosols. We infer that the anthropogenic aerosol contribution is greater for the NH than for the SH, consistent with other studies (1, 3–8, 12, 17, 22–25).

The substantial radiative effect of the naturally occurring sea-salt aerosol is evident over vast areas of the world's oceans, especially in the SH and equatorial areas, which are associated with high surface wind speeds. Sea-salt aerosols exert a greater effect relative to other aerosols in the SH than in the NH. The modeled solar reflection is also governed by the degree to which the sulfate aerosol effect is masked by sea-salt particles. Although the uncertainty in sea-salt mass loading is probably a factor of 3 or more, the uncertainty in its specific extinction, based on present observations of the sub- and supermicrometer size categories, is unlikely to exceed about 30% (26). The importance of sea-salt underscores the need to account for it in aerosol climate forcing considerations, including changes in sea-salt concentration due to secular trends in surface wind speeds (33). In addition to the linkage with sea-salt, wind speed may also affect the surface reflectance of oceans through the Fresnel effect or by producing whitecaps (34).

The precision of the aerosol radiative computations is constrained somewhat by uncertainties in the modeling of global aerosol distributions and the associated optical effects. There remain some regions where the quantitative difference between calculations and observations is likely due to factors other than aerosols such as uncertainties in ocean surface albedo and humidity and satellite retrieval algorithms. In conclusion, the satellite radiation measurements verify from an observational perspective that considerations of the various natural and anthropogenic aerosol species are essential for explaining the measured global clear-sky solar reflection. Although other factors could potentially further improve on the computed solar reflection, there is currently no known cause besides aerosols that will yield the spatial structure and magnitudes necessary to account for the biases in the modeled irradiance patterns. This establishes a definitive role for natural and anthropogenic aerosols in the radiation budget of the global climate system.

References and Notes

1. D. Schimel *et al.*, in *Climate Change 1995: The Science of Climate Change*, J. T. Houghton *et al.*, Eds. (Cambridge Univ. Press, Cambridge, 1996); R. J. Charlson, J. Langner, H. Rodhe, C. B. Leovy, S. G. Warren, *Tellus* **43AB**, 152 (1991).
2. E. P. Shettle and R. W. Fenn, *Technical Paper AFGL-79-0214* (Air Force Geophysics Laboratory, Hanscom Air Force Base, Hanscom, MA, 1979); O. B. Toon and J. B. Pollack, *J. Appl. Meteorol.* **15**, 225 (1976).
3. J. Langner and H. Rodhe, *J. Atmos. Chem.* **13**, 225 (1991).
4. P. Kasibhatla, W. L. Chameides, J. St. John, *J. Geophys. Res.* **102**, 3737 (1997).
5. W. F. Cooke and J. J. N. Wilson, *ibid.* **101**, 19395 (1996).
6. C. Liousse *et al.*, *ibid.*, p. 19411.
7. I. Tegen and I. Fung, *ibid.* **100**, 18707 (1995).
8. I. Tegen *et al.*, *ibid.* **102**, 23895 (1997).
9. S. L. Gong *et al.*, *ibid.*, p. 3819.
10. J. A. Coakley, R. D. Cess, F. Yurevich, *J. Atmos. Sci.* **40**, 116 (1983).
11. E. F. Harrison *et al.*, *J. Geophys. Res.* **95**, 18687 (1990); V. Ramanathan *et al.*, *Science* **243**, 57 (1989).
12. J. M. Haywood and V. Ramaswamy, *J. Geophys. Res.* **103**, 6043 (1998).
13. F. J. Wentz, *IEEE Trans. Geosci. Remote Sensing* **30**, 960 (1997).
14. The radiation scheme used combines the delta-Edgington method with an exponential-sum fitting technique to handle multiple-scattering and molecular absorption (12). The parameterization has been developed and calibrated with high spectral resolution line-by-line adding-doubling solutions of Ramaswamy and Freidenreich [*J. Geophys. Res.* **103**, 23255 (1998)]. [See also S. M. Freidenreich and V. Ramaswamy, *Ninth Conference on Atmospheric Radiation*, Long Beach, CA, American Meteorological Society, February 1997, pp. 129–130; S. M. Freidenreich and V. Ramaswamy, in preparation.]
15. M. D. Glew, P. Hignett, J. P. Taylor, *J. Geophys. Res.*, in press.
16. The methodology of using the Geophysical Fluid Dynamics Laboratory (GFDL) Climate GCM for the particular set of experiments is similar to (12). The aerosol radiative effects do not feedback onto the GCM's dynamics. A single year is sufficient to accurately describe the annual clear-sky irradiances from the GCM because the sensitivity of the TOA irradiance to changes in meteorology (mainly water vapor concentrations) is small, and the prescribed ocean surface reflectance in the GCM does not have any interannual variation.
17. J. M. Haywood *et al.*, *J. Climatol.* **10**, 1562 (1997).
18. P. K. Quinn and D. J. Coffman, *J. Geophys. Res.*, in press.
19. "Low" sea-salt burdens are obtained with the formulation of R. F. Lovett [*Tellus* **30**, 358 (1978)]; "high" sea-salt burdens are obtained with the formulation of H. J. Exton *et al.* [in *Oceanic Whitecaps and Their Role in Air-Sea Exchange Processes*, E. C. Monahan and G. Mac Niocaill, Eds. (Reidel, Hingham, MA, 1986), pp. 195–208]. See also (9). The empirical formulations relate the sea-salt concentration (g/cm^3) to the local surface wind speed (m/s).
20. *WCP. A Preliminary Cloudless Standard Atmosphere for Radiation Computation* (World Meteorological Organization, Geneva, 1986).
21. O. B. Toon, J. B. Pollack, B. N. Khare, *J. Geophys. Res.* **81**, 5733 (1976).
22. I. Tegen, A. A. Lacis, I. Fung, *Nature* **380**, 419 (1996).
23. J. T. Kiehl and B. P. Briegleb, *Science* **260**, 311 (1993).
24. K. Taylor and J. E. Penner, *Nature* **369**, 734 (1994).
25. O. Boucher and T. L. Anderson, *J. Geophys. Res.* **100**, 26117 (1995).
26. From (18), the mean specific extinction at 70% relative humidity of the typically small and large particles constituting the sea-salt aerosol distribution is estimated as 8.7 and 1.9 m^2/g , respectively. The mass concentration in the supermicrometer mode is typically about 10 times (range 6 to 16 times) that in the submicrometer mode. Using the observations in (18), we estimate that the effective specific extinction for the entire distribution considering both the modes varies between 2.3 and 2.9 m^2/g . We adopted a value of 2.5 m^2/g and an asymmetry factor of 0.78 at 0.55 μm for the present calculations. Note that the value of the specific extinction is substantially greater than the one obtained by considering supermicrometer particles only (18).
27. The biases estimated for the clear-sky ERBE reflected solar irradiance fields are estimated to be about 1 W/m^2 or less when averaged over a 2.5° grid ocean box and over monthly-mean time scales; the monthly-mean results are estimated to have a root mean square bias of 2 W/m^2 or less (17). Bias estimates for zonal and global means are likely to be even smaller than for the regional means.
28. S. Cusack, A. Slingo, J. M. Edwards, M. Wild, Q. J. R. Meteorol. Soc. **124**, 2181 (1998); J. T. Kiehl, J. J. Hack, J. W. Hurrell, *J. Climatol.* **11**, 1151 (1998).
29. As an indication of the sensitivity to uncertainties in water vapor, additional calculations for July 1988, with European Center for Medium Range Weather Forecasts (ECMWF) assimilated analyses of water vapor in place of the GCM water vapor fields, revealed differences of less than 20% from the biases shown in Fig. 1A.
30. Offline calculations performed with daily-mean rather than monthly-mean wind speeds yielded sea-salt concentrations that differ by ~15% on average. This difference is much smaller than the uncertainty in the mass-loading versus wind speed relation (19).
31. B. J. Soden and V. Ramaswamy, *Geophys. Res. Lett.* **25**, 2149 (1998).
32. D. M. Murphy *et al.*, *Nature* **392**, 62 (1998). Their measurements at a remote location indicate that much of the sulfur is on particles that also contain sea-salt. In effect, sea-salt aerosols provide reac-
- tion sites for the conversion of SO_2 to sulfate. The connection between sea-salt and sulfur cycles is also discussed by H. Sievering *et al.* [*ibid.* **360**, 571 (1992)] and N. A. Clegg and R. Toumi [*J. Geophys. Res.* **103**, 31095 (1998)]. Thus, for particles in the radiatively important size regime, the radiative contributions of sea-salt and sulfur may be linked. P. Quinn *et al.* [*ibid.*, p. 16547] point out that sea-salt controls the aerosol optical properties in the southern ocean in both the sub- and supermicrometer modes.
33. J. Latham and M. H. Smith, *Nature* **347**, 372 (1990).
34. The radiative effects of wind speed upon the sea-surface reflectance can be accounted for by including both a parameterization for the Fresnel effect [J. E. Hansen *et al.*, *Mon. Weather Rev.* **4**, 609 (1983)] and the effects of whitecaps [E. C. Monahan, *J. Phys. Oceanogr.* **1**, 139 (1971)]. Calculations performed with the assumption that the whitecaps are diffuse reflectors with an albedo of 0.6 suggest that the global surface reflectance is likely to decrease rather than increase as a function of wind speed; this cannot, therefore, explain the bias between model and observed reflected irradiances at the TOA seen in Fig. 1A.
35. We thank P. Kasibhatla and J. Langner for providing the sulfate climatologies, W. Cooke for providing the black carbon climatologies, I. Tegen for providing the dust climatologies, the NASA/Langley Distributed Active Archive Center (DAAC) for providing the ERBE data, the NASA/Jet Propulsion Laboratory DAAC for providing the SSMI data, and A. Broccoli, D. Schwarzkopf, R. Stouffer, and two anonymous reviewers for their comments and suggestions.

12 November 1998; accepted 26 January 1999

Lu-Hf Isotope Systematics of Garnet Pyroxenites from Beni Bousera, Morocco: Implications for Basalt Origin

Janne Blichert-Toft,^{1*} Francis Albarède,¹ Jacques Kornprobst²

Six garnet pyroxenites from Beni Bousera, Morocco, yield a mean lutetium-hafnium age of 25 ± 1 million years ago and show a wide range in hafnium isotope compositions ($\epsilon_{\text{Hf}} = -9$ to $+42$ 25 million years ago), which exceeds that of known basalts (0 to $+25$). Therefore, primary melts of garnet pyroxenites cannot be the source of basalts. The upper mantle may be an aggregate of pyroxenites that were left by the melting of oceanic crust at subduction zones and peridotites that were contaminated by the percolation of melts from these pyroxenites. As a consequence, the concept of geochemical heterogeneities as passive tracers is inadequate. Measured lutetium-hafnium partitioning of natural minerals requires a reassessment of some experimental work relevant to mantle melting in the presence of garnet.

An upper mantle composition of depleted lherzolite with small zones of more mafic and fertile pyroxenite is consistent with the subduction of oceanic crust and the ubiquitous presence of pyroxenite layers in high-temperature

peridotite massifs (1). The isotope geochemistry of Hf (2) and Th (3) seems to require the presence of residual garnet in the melting zone, even beneath the mid-ocean ridges (4). The compositional variability of oceanic basalts from mid-ocean ridge basalts (MORBs) to ocean island basalts could reflect either variable contributions of garnet pyroxenites to their source (5–8) or a broad pressure range of melting in a relatively homogeneous mantle (9, 10). The Nd-Hf isotopic properties of peridotite inclusions from the western United States have

¹Ecole Normale Supérieure de Lyon and CNRS, 46 Allée d'Italie, 69364 Lyon Cedex 7, France. ²L'Unité Mixte de Recherche CNRS "Magmas et Volcans," Observatoire de Physique du Globe de Clermont-Ferrand, 5 rue Kessler, 63038 Clermont-Ferrand, France.

*To whom correspondence should be addressed.